ACS OMEGA

Open Access

http://pubs.acs.org/journal/acsodf

Article

Facile Synthesis of Poly(methyl methacrylate) Silica Nanocomposite Monolith by In Situ Free Radical Polymerization of Methyl Methacrylate in the Presence of Functionalized Silica Nanoparticles

Grigori Oehl, Naofumi Naga,* and Gerhard Ziegmann

Cite This: *ACS Omega* 2024, 9, 16279−16287

Read Online

ACCESS | Metrics & More | Article Recommendations | Supporting Information

ABSTRACT: Novel porous poly(methyl methacrylate) (PMMA) silica nanocomposites have been produced by utilization of polymerization-induced phase separation in a simple one-pot approach. A facile free radical polymerization of MMA in the presence of surface methacrylate-functionalized silica nanoparticles was carried out in ethanol-based solvents, successfully producing novel, morphologically designable porous nanocomposite monoliths. Differing from standard free radical polymerization in solution, a mixture of good and poor solvents (ethanol/*N*,*N*-dimethylformamide ratio) for the resulting polymer was used to trigger spinodal phase separation. The influence of monomer concentration, as well as solvent composition, on the morphology of the resulting porous polymers has been investigated. Porous monolith structures composed of connected particles and co-continuous morphologies were observed under a scanning electron microscope depending on the polymerization conditions. The resulting polymers were insoluble and showed swelling characteristics in some organic solvents that are capable of dissolving regular PMMA, indicating covalent bonds between the functionalized silica nanoparticles and the polymer chains. The presence of silica particles in the final polymer was proven via an ATR-IR analysis. The glass transition temperature of the present PMMA−silica nanocomposite was higher than that of the conventional PMMA. The porous polymer immersed in a mixed organic solvent showed coloration induced by the Christiansen effect.

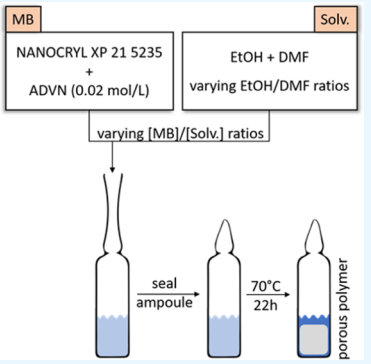

INTRODUCTION

Poly(methyl methacrylate) (PMMA) is a versatile polymeric material that has proven to be popular over several decades with global sales in excess of $4 billion annually.[1] PMMA is primarily used in the construction, automotive sectors,[2] and manufacturing industry as granulate,[3] but it is certainly not restricted to these markets. Another example of current applications lies in the medical sector, within dental technology in particular.[4] More niche use cases can be found in hybrid layups of PMMA and mineral glass[5] or in creative furniture products,[6] as well as in the cosmetics industry.[6]

The commercial-scale production of PMMA is still mainly carried out by radical polymerization, although anionic and living polymerizations sometimes find application as well, albeit less often.[3,7] The utilization of emulsion polymerization, solution polymerization, and bulk polymerization are present to achieve PMMA in different shapes, from sheets and panes to powder for further processing.[8] In the past, extensive research has been carried out on various polymerization techniques, including conventional radical, atom transfer radical (ATRP), reversible addition−fragmentation chain transfer radical (RAFT), coordination-based polymerization, and so forth, in order to achieve high-molecular-weight PMMA with low dispersity for optimized mechanical properties.[9] A possible adaptation of these techniques depends on the financial viability, including the utilized reagents in large-scale production. The vast field of available options offers the possibility to select a process based on application to optimize each product toward its requirements.

PMMA is also capable of being highly functionalized by several methods. Modification on the methoxy group of the polymer[10] leads to special applications like in DNA microarrays[11] or as a substrate for drug delivery systems.[12] Additionally, PMMA offers the ability to be utilized as a base polymer for composite materials, e.g., in combination with SiO_2 particles[13] to improve the thermal stability[14] and mechanical properties.[15] Multidimensional processing of PMMA is also usable to expand the application, e.g., in development of filters composed of PMMA-based materials. Zulfikar et al. showed that the addition of tetraethoxyorthosilane to prepolymerized PMMA yields promising results in a wide variety of membranes with different permeabilities.[16] A similar, yet simpler approach was reported by Srirama et al. to

Received: December 25, 2023
Revised: February 26, 2024
Accepted: March 1, 2024
Published: March 29, 2024

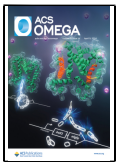

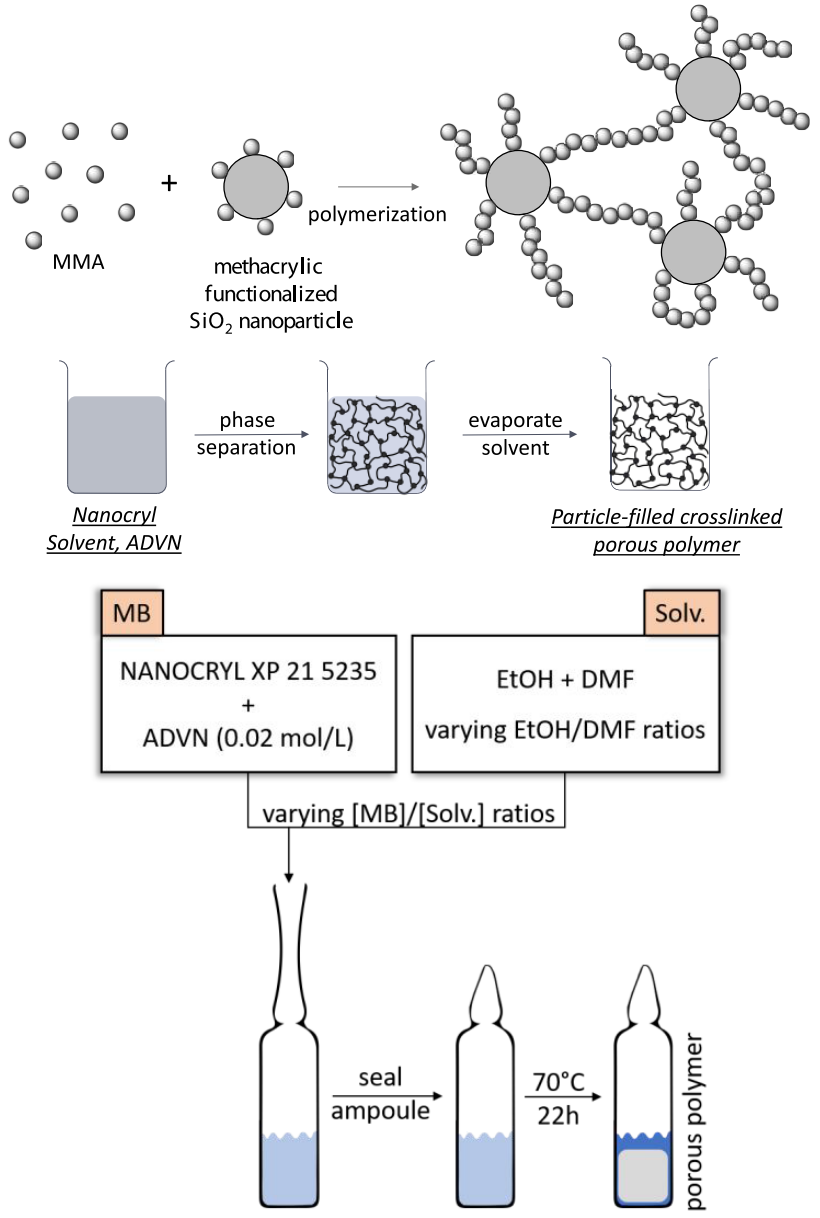

Figure 1. Schematic diagram explaining the crucial steps in order to synthesize PMMA−silica nanocomposite monoliths.

demonstrate the oil−water separating capabilities of porous PMMA/SiO_2 infused filter papers.[17] A different approach to acquire porous PMMA is creating a scaffold from chitosan-oligosaccharide via freeze-drying and filling this porous structure with a polymerizing mixture of MMA, cross-linkers, and initiators.[18] Furthermore, cooling of PMMA solution in a mixture of ethanol (EtOH) and water at elevated temperatures leads to phase separation and induces porous structures.[19] In situ synthesis of porous PMMA with a bicontinuous structure via spinodal decomposition has some advantages for the processing of PMMA.[20] Addition of polyethylene glycol showed promising capabilities as porogen (pore generator) for in situ synthesis of microporous PMMA samples.[21] These phase separations can further lead to interesting effects like wavelength-dependent scattering of light, shown by Sicher et al. for PS−PMMA, where the polymer was swollen in a monomer, resulting in a phase separation during polymerization.[22] Another work that is closely related to this topic has been carried out by Chinthamanipeta et al., who created well-defined PMMA-SiO_2 nanocomposites in a covalently bonded state via RAFT polymerization, showing slightly improved overall mechanical and thermal properties compared to bulk PMMA.[23]

The research presented in this paper focuses on utilizing industry-leading, conventional radical polymerization and grafting-through strategies in order to create a facile method resulting in covalently bonded PMMA−silica nanocomposite monoliths with steerable morphologies. Innovative to this approach is the simultaneous application of SiO_2 nanoparticles in a polymerization-induced phase separation process, taking parts of the aforementioned work from Suzuki and Chinthamanipeta as a basis.[21,23] Hence, this novel one-pot method combines conventional radical polymerization with a grafting-through mechanism on premodified, commercially available nanoparticles, allowing rapid industrial application of these polymerization-induced phase-separation-based monoliths.

https://doi.org/10.1021/acsomega.3c10338
ACS Omega 2024, 9, 16279−16287

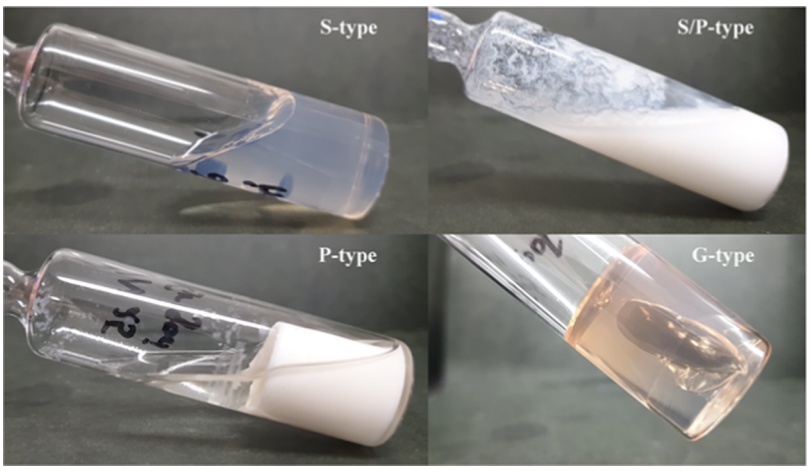

Figure 2. Exemplary pictures visualizing the different sample types (P, porous polymer; G, solid gel type; S, viscous solution).

Regarding possible applications, the resulting porous structures could be used in many fields where porous solids are already present. This includes filtering different media regarding size or polarity, as a base material for membranes or generally as structured surfaces like those discussed above. The good biocompatibility of PMMA and incorporation of nanoparticles broadens this field even further. Taking a look at the work of Xu et al., drug delivery systems of self-assembling block polymers containing silica nanocapsules filled with drugs for cancer or Covid treatment show promising novel applications, although their approach also benefits from stimuli-responsivity, which is not included in this work.[24−26] Modification of the methoxy group allows even further extension of these possible fields of application, opening up toward life-science applications like cell-separation (i.e., Fab-TACS technology from IBA) just to name one example in this field.[10,27]

MATERIALS AND METHODS

As aforementioned, the base material for the studies presented in this paper is a commercially available MMA−silica nanoparticle mixture, where the surface of said particles is pretreated by the manufacturer in order to have groups present on their surface. This mixture (Nanocryl XP 21 5235) was gracefully supplied by *Evonik Industries* and has a particle loading of 30.5 ± 0.35 wt % with a particle diameter of 20 nm (measured by dynamic light scattering (DLS), see Supporting Information Figure S1). Grafting density has not been determined, but thermogravimetric analysis on predried particles showed an organic loading of approximately 6.5 ± 0.1 wt % (Figure S2), where the organic origin of the mass loss was proven via attenuated total reflection infrared spectroscopy (ATR-IR) (Figure S3). Furthermore, this suspension is prestabilized with 0.1 wt % 4-methoxyphenol and was used without further purification.

The addition of 2,2′-azobis(2,4-dimethyl-valeronitrile) (ADVN) (0.02 mol/L) to this commercial suspension leads to a reactive masterbatch, referred to as MB in this work (see Figure 1—MB). Combinations of MB with different EtOH/*N*,*N*- dimethylformamide (DMF) solvent mixtures were created and sealed in airtight ampules (Solv. in Figure 1). The polymerization occurred at 70 °C for 22 h.

Cleaning of the resulting solid samples has been carried out by thoroughly rinsing in 10-fold of methanol for 24 h three times, along with drying the sample under vacuum at room temperature after each rinse.

In order to characterize the nanoparticles regarding their usability to create covalent bonds with MMA as well as proofing their existence in the final porous product, ATR-IR measurements were carried out on a Bruker Vertex 70 V with a platinum ATR unit. Measurements have been carried out in a range between 400 and 4000 cm^{-1} at a resolution of 4 cm^{-1}, summing up 100 scans for averaging.

Scanning electron microscopy (SEM) was carried out on a JEOL JSM-7610F FE-SEM instrument with an acceleration voltage of 3 kV in backscatter imaging mode. The samples had to be coated with a thin layer of gold in a plasma sputter coater (JEOL DII-29010SCTR) to ensure conductivity and minimize charging effects. A coating time of 30 s with a 20 mm sample target distance achieved optimal results. Validation of the pore size estimations from SEM images has been carried out on a few representative samples via mercury porosimetry on porosimeters Pascal 140 and Pascal 240 from Thermo Scientific.

In order to characterize the surface area of the samples, nitrogen adsorption tests according to Brunauer−Emmett−Teller (BET) theory were conducted on a Belsorp II mini from MicrotracBEL. Pretreatment took place at 125 °C under vacuum to ensure dryness of every sample. Cooling during measurement is realized with liquid nitrogen, and the measurement procedure went fully automated.

The expected cross-linking of polymers usually results in a lower susceptibility to solvents. In order to characterize this effect, geometrical swelling of thoroughly predried (5 h at 40 °C in vacuo) cubic (approximately 0.75 cm) samples was measured after storage in common solvents for 18 h. The solvents of choice, water, hexane, ethanol, methanol, and *N*,*N*-dimethylformamide were selected.

Thermal properties like glass transition temperature and decomposition range were first determined with thermogravimetric differential thermal analysis (TG-DTA) and later verified via thermogravimetric analysis (TGA) and differential scanning calorimetry (DSC) measurements on a Bruker AXS, a TA Instruments Q5000 IR, and a TA Instruments Q2000 respectively. For DTA, the specimens were heated from room temperature to 500 °C at a heating rate of 20 K min^{-1} under an argon atmosphere. For TGA, a heating rate of 10 K min^{-1} was used. Up to 600 °C, nitrogen was used as inert gas and

https://doi.org/10.1021/acsomega.3c10338
ACS Omega 2024, 9, 16279−16287

replaced with air for the following 200 up to 800 °C for oxidation analysis. The DSC measurements were also conducted with a heating rate of 10 K min^{-1} in a heat−cool−heat cycle following the pattern 0−140−0−200 °C, where second heat was used for material analysis in order to exclude material handling effects.

RESULTS AND DISCUSSION

The radical polymerization of Nanocryl XP 21 5235 promotes the copolymerization of MMA the surface methacrylate-functionalized silica nanoparticles and forms the PMMA networks cross-linked by the nanosilica. In order to control the phase separation, mixtures of DMF as the good solvent and EtOH as the poor solvent were prepared in different containers with varying ratios. A matrix illustrating these ratios, as well as the photos of some typical resulting samples, is shown in Figure 2 (Figure S4) and Table 1. Photos of all of the samples

Table 1. Resulting Sample Types (P: Porous Polymer; G: Solid Gel Type; S: Viscous Solution; -: Not Tested), Color-Coded by Extraction Feasibility (Green: Direct Extraction; Yellow: Sticky Sample Solidified after Solvent Exchange; Orange: Partial Sample Loss as Precipitate; Gray: No Porous Polymer)

Sample types		Masterbatch concentration in wt%					
		10	20	30	40	50	60
EtOH / DMF ratio in wt%	100/0	P	P	P	P	P	P
	90/10	S/P	S/P	P	P	P	P
	80/20	S/P	S/P	P	P	P	P
	70/30	S	S	S	P/G	G	G
	60/40	S	S	S	S	G	G
	40/60	S	S	S	S	-	-
	20/80	S	S	S	S	-	-
	0/100	S	S	S	S	-	-

are to be found in Supporting Information Figure S3. The nomenclature M#(E#D#) will be used henceforth, where M# represents the amount of masterbatch (MB) in a mixture of EtOH (E#) in DMF (D#). Exemplarily, M60(E90D10) refers to 60 wt % MB in a solvent mixture of 90 wt % EtOH and 10 wt % DMF.

The composition of solvent mixtures and the MB concentration strongly affected the types of the samples. Four different types of samples, illustrated in Table 1, can be grouped according to criteria described in the following.

The gray zone marks samples, where an extraction of a solid was not feasible, and the polymerization led to an increase in viscosity but did not show apparent phase separation (see Figure 2 "S-type"). With increasing the MB concentration, the viscosity became higher, whereas the EtOH/DMF ratio had a less dominant, visually nonobservable influence on the viscosity. It seems plausible that the high amount of good solvent DMF in these mixtures hinders solidification to an extent, where only an extremely swollen state is apparent after polymerization; thus, a viscous behavior can be seen. As porous polymers are the focus of this research, these samples were disregarded in future analysis.

The second largest group (green zone) represents easily extractable fully phase-separated porous polymers (see Figure 2 "P-type"). Regarding the formation of the porous structures, a rapid transition from the liquid to solid phase has been observed. These samples will be in focus for this paper, and the following discussions fully refer to the green zone.

In between lies the orange zone, where phase separation is not sufficient, and the samples show characteristics of partly precipitated polymer that can be easily fragmented (see Figure 2 "S/P-type"). The low MB concentration as well as moderate content of a good solvent led to separated domains during curing. These domains do not fully connect during phase separation, and therefore, building of a solid block like with P-type samples does not occur.

In the reactions with high MB concentration and a medium DMF content (yellow zone), the resulting samples represent a fully gel-type polymer (see Figure 2 "G-type"). With this type, the samples enter a swollen state that is similar to S-type samples but due to the higher MB concentration rich in polymer phase, leading to a state that can be transferred to a P-type by adding a poor solvent like EtOH or MeOH during the washing phase.

As seen in Figure 2, G-type samples show a distinct discoloration, which is also observable in the P-types with similar composition. This could be due to dispersion effects of the nanoparticles in the surrounding solvent mixture, as the effect disappears after replacing and removing the solvents.

The porous structures were created by polymerization-induced phase separation. Normally, the polymerization of a monofunctional vinyl monomer is conducted in a good solvent, which shows good solubility for the resulting polymer, to obtain a high-molecular-weight polymer with good yield in the homogeneous reaction system. By contrast, with the corresponding polymerization in a poor solvent, in which the resulting polymer is insoluble, the precipitates are formed as the polymerization progresses caused by the decrease in the solubility of the resulting polymer with increase in the molecular weight. In the case of the network polymer formed by a (co)polymerization of a multifunctional vinyl monomer, the gel was generated when the formation of the polymer network is completed before the phase separation as shown in Figure 2 "G-type". The viscous solution (Figure 2 "S-type") would be obtained due to the insufficient formation of the infinite-polymer network. When the mutually immiscible phases of the solvent and the polymer can coexist in the reaction system during the polymerization, the porous polymer composed by the polymer backbone and the solvent is successfully obtained as shown in Figure 2 "P-type".

In order to prove the existence of the nanoparticles in the final porous composite, ATR-IR spectra on representative samples have been acquired. Figure 3 shows an excerpt highlighting the interesting areas of C═O valence at 1722 cm^{-1} representing the strongest member of PMMA contribution, as well as two Si−O and Si−O−Si bands at 464 and 1086 cm^{-1}.[28] Comparison to the neat particles (Figure S3) highlights the dominance of silicas IR activity, which overpowers the PMMA bands in the composite to a great extent. Energy-dispersive X-ray spectroscopy (EDX) also showed silica peaks but less prominent and was therefore not included in this paper but shall be mentioned at this point. Additionally, there is no C═C signal at around 1640 cm^{-1}, indicating a fully cured composite with close to no reactive groups, which can be expected from a solution-based polymerization.

Scanning electron microscopy (SEM) images of the dried P-type samples in backscatter imaging mode are shown in Figure 4 (Figures S5 and S6). Taking the SEM images on porous morphologies into account, spinodal decomposition as a nucleation free spontaneous phase separation seems to be

https://doi.org/10.1021/acsomega.3c10338
ACS Omega 2024, 9, 16279−16287

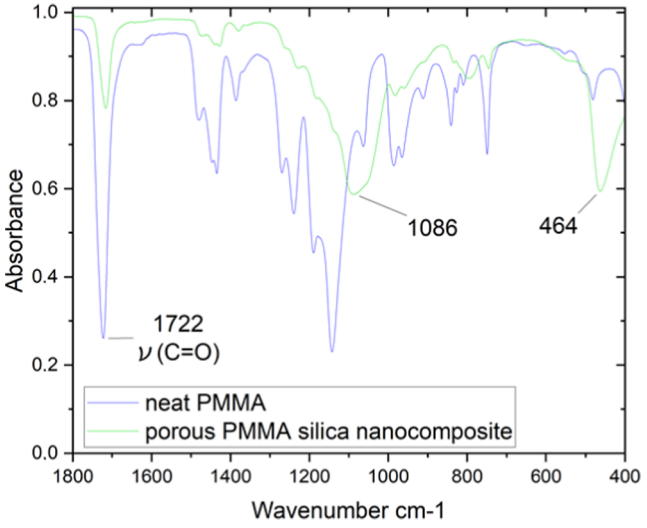

Figure 3. ATR-IR spectra for neat PMMA (blue) and representative porous PMMA−silica nanocomposite M60(E90D10) (green).

the most reasonable mechanism leading to the present porous structures (Figure S7). In the early stage of the phase separation, the co-continuous monolithic structure is formed. The progress of the phase separation transfers the monolithic structure to connected particles due to interfacial tension. As a general observation, the samples with an MB concentration below 30% consisted of small, interconnected particles (Figure 4A,D,G), whereas higher MB concentrations yielded co-continuous morphologies. This is believed to be caused by the higher content of the interconnectable polymer fixed at the early stage of the phase separation for high MB samples, leading to a closed morphology. By contrast, the decomposition of samples with low MB content happens without connection due to the fixation of the phase transfer at the late stage of the phase separation. In both cases, the high rate of spinodal decomposition does not allow for significant nucleus growth and therefore no change in morphology from the dissolved state to the solid state. The transition between these two opposing structures can be seen in Figure 4, where MB concentration increases from left to right for different solvent mixture-based samples.

Regarding solvent influence, for reactions with very low MB concentrations (below 20 wt %), the increase of the DMF ratio changes the particle size marginally, leading to bimodal particle distributions as shown in Figure 4A,D,G. Here, the morphology itself was not influenced by the solvent's composition. For porous polymers obtained in the reactions with high MB concentrations, the composition of the EtOH/DMF mixed solvent does not change the monolithic porous structure in a meaningful way either. This leads to the conclusion that the structures and pore sizes of samples with an MB concentration of 40 wt % and above are only related to the amount of MB, regardless of the solvent mixture.

By contrast, in the reactions with moderate MB concentrations, especially 30 wt %, significant morphological changes were observed by increasing the DMF ratio in the solvent mixture. M30(**E100D0**) (Figure 4B) shows a co-continuous monolithic structure, whereas M30(**E80D20**) (Figure 4H) is represented by connected particles. The sample between those compositions (Figure 4E—M30(E90D10)) shows a unique three-dimensional network of a few micrometers in both the polymer thickness and void distance. Hence, this sample represents a transition point between the two dominant morphologies. The reactive batch is at a tipping point between interconnected particles and co-continuous monolith, leading to this unique shape.

Regarding particle sizes, ranges from around 100 nm up to approximately 1 μm have been observed, where larger particles could be seen at higher MB concentrations. The pore sizes of the co-continuous monolithic structures range from ∼200 nm up to ∼5 μm, with a tendency toward smaller pores at higher MB concentrations. SEM images of all of the P-type samples are summarized in Supporting Information Figures S5 and S6.

In order to verify the SEM-based pore size approximations, mercury porosimetry was carried out on representative samples. Figure 5 illustrates the small pores around 700 nm

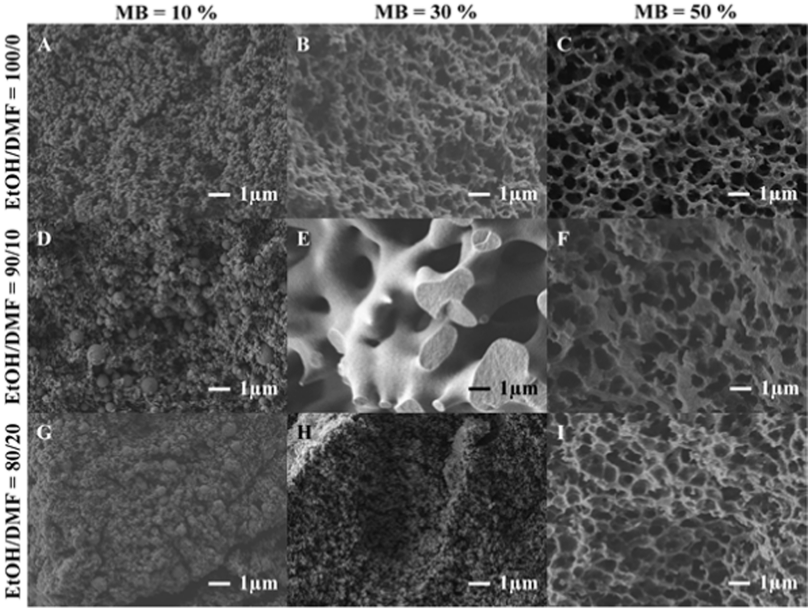

Figure 4. SEM images of PMM−silica nanocomposite monoliths.

https://doi.org/10.1021/acsomega.3c10338
ACS Omega 2024, 9, 16279−16287

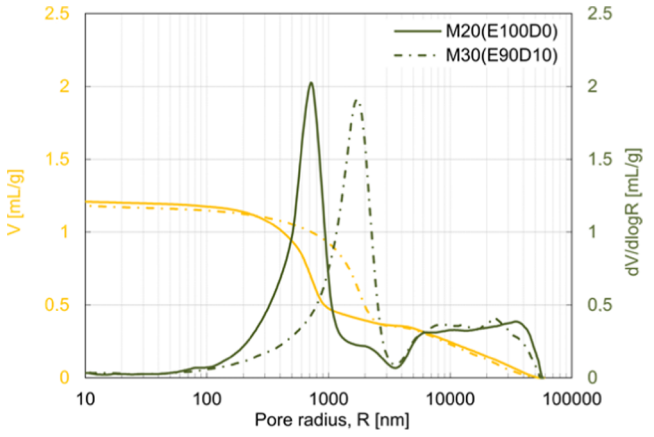

Figure 5. Mercury porosimetry measurements on representative samples (full line: structure with connected particles; dotted line: co-continuous structure).

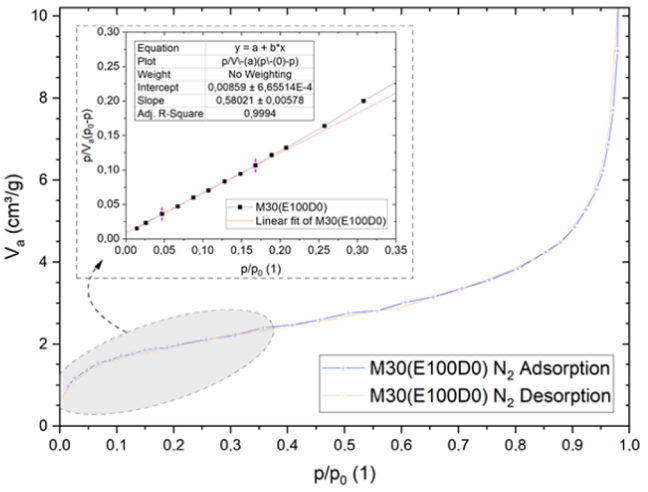

Figure 6. Exemplary nitrogen adsorption−desorption curve and BET analysis graph, including linear regression for an M30(E100D0) sample.

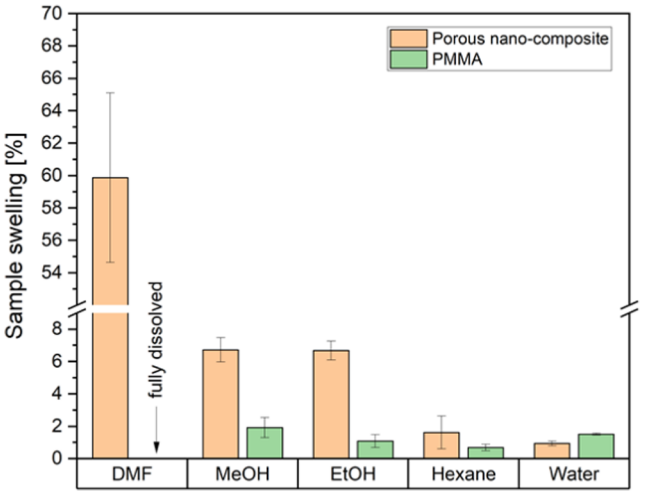

Figure 7. Averaged volume swelling behavior of porous PMMA−silica nanocomposite monolith M60(E90D10) (orange) and bulk PMMA (green).

for M20(E100D0) and rather large pores (approximately 1700 nm) for the co-continuous structure M30(E90D10). The area above 5000 nm is believed to be representing the filling of the intermediate particle volume and surface areas and does not directly represent the pore sizes and volumes and thus was neglected in pore size determination. The overall results align quite well with the already mentioned pore sizes obtained via SEM images and therefore support the optical determination method.

As expected, the density of the samples aligns with structures observed via SEM and is lowest for small MB concentrations, as well as rising with it in a range from as low as 0.29 up to 0.92 g cm^{-3}. Increased DMF content also contributes to a higher density, although to a much lesser extent. Mechanical strength follows the same pattern but can only be reported as subjective resistance to cutting in the realm. The obtained porous polymers were not broken by the compression test under 500N, and it was impossible to evaluate the mechanical properties, such as Young's modulus and breaking stress−strain, of the porous polymers quantitatively.

The surface areas of the samples were evaluated by nitrogen adsorption tests according to the Brunauer−Emmett−Teller (BET) theory. The results were not consistently measurable on all samples, but showed small surface areas for porous polymers around 1 and up to 10 m^2g^{-1} in average. Taking a look at an exemplary adsorption−desorption curve (see Figure 6), the curve shape follows "type II" according to ISO 9277.[29] The linear regression between 0.05 and 0.175 also illustrates the applicability of BET theory, proving the small but present pore size. The minor deviation from the ideal linear BET curve above 0.2 is disregarded at this point but will be examined in upcoming research on this topic. For verification, alternative measurement techniques like mercury intrusion porosimetry or nano-CT measurements, exceeding the aim of this paper, shall be applied in the future.

The solvent swelling behavior of the PMMA−silica nanocomposite monoliths was investigated. The samples were vacuum-dried at 40 °C for 5 h, and the dimensions and mass were measured, cubic (approximately 0.75 cm), just before the swelling test. The samples were soaked in the respective solvent at least 10-fold to sample mass at room temperature. The mean values are presented in the following, as deviations were small among the samples. Figure 7 illustrates the geometrical swelling of the samples after storage in common solvents for 18 h to complete the equilibrium swelling. Nonporous bulk PMMA without SiO_2 nanoparticles was also analyzed for comparison. The difference in the swelling for hexane and water between the porous and nonporous samples is negligible (around 1−2%). The porous polymer showed a higher swelling ratio in the absorption of both methyl alcohol (MeOH) and EtOH compared to bulk PMMA. DMF, which is a good solvent for PMMA, fully dissolved the bulk PMMA. However, the porous nanocomposite was drastically swelled in DMF within a few hours, indicating the chemical 3D-cross-linking via the functionalized nanoparticles. These results can be explained by the solubility parameters (SP) of PMMA and solvents used. The solubility parameters of PMMA, DMF, MeOH, EtOH, hexane, and water are 9.2, 12.0, 14.5, 12.7, 7.3, and 23.4 (cal. $cm^{-3})^{1/2}$. The closed SP values between PMMA and the solvent indicate the high solubility of PMMA and high miscibility with the PMMA−silica nanocomposite network. The small difference of SP values (ΔSP) between PMMA and DMF (ΔSP: 2.8 (cal. $cm^{-3})^{1/2}$), which should make it possible to infiltrate DMF into the PMMA−silica nanocomposite network. Quick and high swelling of the porous polymers,

https://doi.org/10.1021/acsomega.3c10338
ACS Omega 2024, 9, 16279−16287

about 60 vol %, in DMF should be derived from the higher miscibility between PMMA in the polymer network. The relatively small ΔSP values between PMMA and MeOH (5.3 (cal. $cm^{-3})^{1/2}$) and EtOH (3.5 (cal. $cm^{-3})^{1/2}$) should cause the low but clear swelling of the porous polymers, about 6 vol %, in these solvents.

Thermogravimetric differential thermal analysis (TG-DTA) measurements were carried out on a Bruker AXS from room temperature to 500 °C at a heating rate of 20 K min^{-1} on samples of 10 mg under an argon atmosphere. An exemplary TG-DTA profile of M60(E90D10) is shown in Figure 8. The

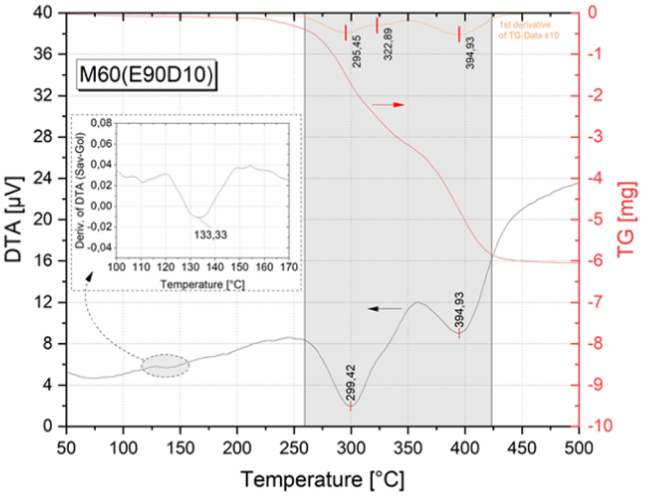

Figure 8. TG-DTA thermograms (exo. down) with 1st derivative of TG-data magnified 10 times in orange of a PMMA−silica nanocomposite monolith M60(E90D10).

DTA data, black (bottom), show an exothermic transition area at around 130 °C, as well as a decomposition in the range of 250 up to 425 °C with two distinct exothermic peaks. The data around the point of interest have been smoothed using a Savitzky−Golay filter to obtain a more precise insight. As a verification for the decomposition temperatures deducted from the DTA signals, the derivatives of TG signals were also smoothed using a Savitzky−Golay filter, and the resulting peaks were included in further data evaluation. In Figure 8, this is represented by the topmost (orange) curve scaled to fit with a magnification factor of 10.

Two characteristic peaks derived from the decomposition of PMMA can be observed at 294.8 ± 1.9 and 388.6 ± 4.3 °C, respectively. The first temperature fits to the literature values of neat PMMA as reported by Nikolaidis et al.[31] and Ferriol et al.,[32] as well as toward the bulk reference from this work as summarized in Tables S1 and S2. Regarding the second peak, a higher value compared to that of neat PMMA is observable.

Selective TGA measurements were able to support this trend, showing the effect of the particle incorporation and cross-linking on thermal degradation that has been reported in previous work, although be it to a lesser extent in this work (Figure 9).

In addition, TGA revealed a later onset temperature for decomposition, as shown in Figure 9 which is also believed to be due to particle incorporation and cross-linking effects. Additionally, a small dent at around 325 °C is detected in both the DTA and TGA plots, especially visible in the derivative in Figure 8 (orange, topmost curve). This might correspond to silica particles debonding from the PMMA network. However,

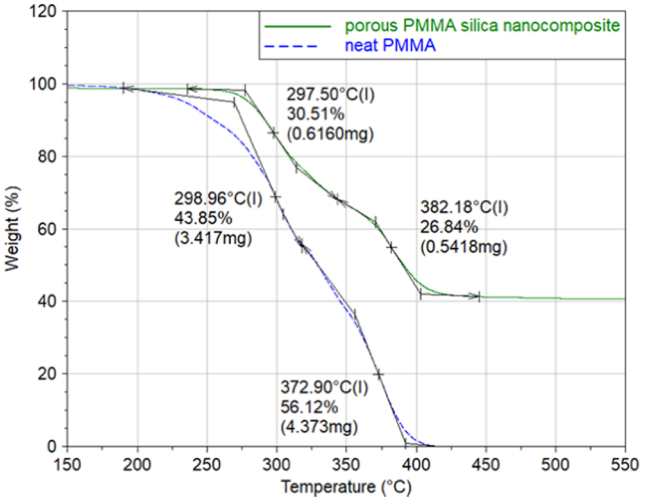

Figure 9. TGA thermogram comparing neat PMMA (blue, dashed line) with an exemplary porous PMMA−silica nanocomposite M20(E90D10) (green, solid line).

further investigations need to be carried out to examine the actual cause of this anomaly.

The aforementioned transition area at 133.0 ± 1.2 °C (measured via DTA) was apparent for all samples and first believed to be representing glass transition, but being exothermic and rather high in temperature compared to standard references of neat, free radical polymerized PMMA (e.g., by Thompson[30]), an exothermic postcuring is believed to happen at this temperature. Utilization of DSC measurements for verification on few samples supports this thesis further (Figure S8), leading to glass transition determination from the second heat of DSC specimens. Figure 10 shows an exemplary comparison between a neat PMMA sample and a porous PMMA−silica nanocomposite in DSC measurements during second heating, where the glass transition point is evaluated for each sample according to the infliction point method. As to be seen, neat PMMA aligns perfectly with the literature range, whereas the novel porous nanocomposite shows a significantly

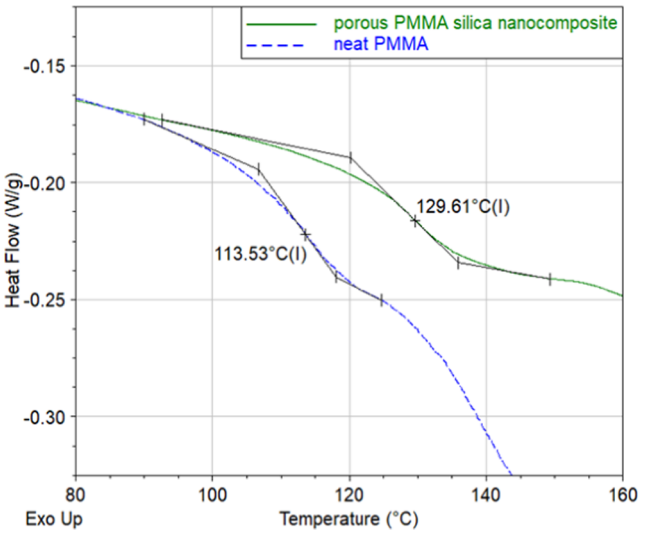

Figure 10. DSC data comparing neat PMMA (blue, dashed line) with exemplary porous PMMA−silica nanocomposite M60(E90D10) (green, solid line).

https://doi.org/10.1021/acsomega.3c10338
ACS Omega 2024, 9, 16279−16287

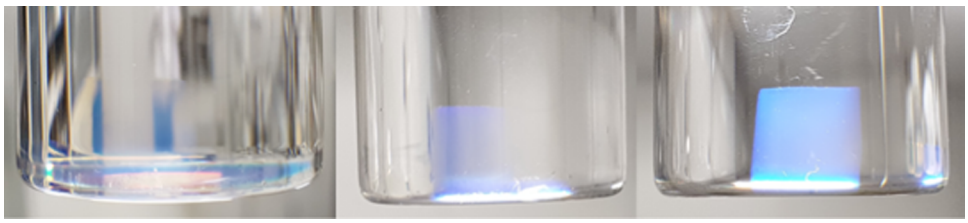

Figure 11. Coloration of a porous PMMA−silica nanocomposite monolith M30(E90D10) submerged in a mixture of toluene, cis-decalin, and cyclohexane illuminated from different angles.

higher transition value, as expected from previous work on nonporous silica nanocomposites.

Light scattering effects of the PMMA−silica nanocomposite monolith were expected in solvents with a refractive index close to that of PMMA due to the porous nature of the composite samples as well as the small particles. Precise control of the refractive index of a mixture solvent of toluene, cis-decalin, and cyclohexane (79.3, 12.2, 8.5 vol % with an approximative refractive index of 1.489, which is close to that of PMMA (1.49)) led to the exact effect as shown in Figure 11. The coloration of the porous polymer in the solvent mixture is derived from the Christiansen effect.[33,34] The visible light blue should be the scattered light with a complementary color to the transmitted light.

CONCLUSIONS

In conclusion, the presented work provides a facile method to produce porous PMMA−silica nanocomposite monoliths, where the combination of PMMA and silica nanoparticles in order to produce porous structures is rather unique. The chemically cross-linking nature of the base material aids the pore generation process as well as supports mechanical stability. Latter was subjectively determined and well observable due to the significant rigidity of the samples leading to minor difficulties in sample preparation compared to standard porous materials. The morphology of the porous structure can be controlled by the concentration of reactive masterbatch in its solvents as well as the composition of the solvent mixtures themselves. The resulting nanocomposite monolith showed high swelling behavior in common solvents that are able to dissolve neat PMMA. The glass transition temperature and heat stability are also elevated. Especially the 3D-network formation, initiated on the surface modified nanosilica, explains these property gains. All of the PMMA−silica nanocomposite monoliths are stable under atmospheric conditions for more than 1 year judging from their appearance. The differences in the molecular structure studied by FT-IR spectroscopy and the porous morphology observed by SEM were rarely observed after about one year.

Regarding future work, functionalization of the polymer surface of the PMMA−silica nanocomposite monolith could expand the application domains of the resulting polymer. Additional investigations to study the effect of the morphology on the various physical properties, such as mechanical properties, with a higher power testing machine, permeability of gases and liquids, thermal conductivity, stability under accelerated exposure test, as well as optimizations on the process parameters like curing temperature or reaction time, are currently in progress, and the results will be reported when available.

ASSOCIATED CONTENT

Supporting Information

The Supporting Information is available free of charge at https://pubs.acs.org/doi/10.1021/acsomega.3c10338.

DLS measurement on Nanocryl XP 21 5235; pictures of prepared samples (still sealed in ampules) for reference to discoloration and phase separation; FE-SEM images of all phase-separated samples at 2000× and 10,000× magnification; and results of TG-DTA measurements in tabular form (PDF)

AUTHOR INFORMATION

Corresponding Author

Naofumi Naga − *Department of Applied Chemistry, College of Engineering and Graduate School of Engineering and Science, Shibaura Institute of Technology, Tokyo 135-8548, Japan;* orcid.org/0000-0003-0695-5011; Email: nnaga@sic.shibaura-it.ac.jp

Authors

Grigori Oehl − *Clausthal Centre for Material Technology, Clausthal University of Technology, 38678 Clausthal-Zellerfeld, Germany; Department of Applied Chemistry, College of Engineering and Graduate School of Engineering and Science, Shibaura Institute of Technology, Tokyo 135-8548, Japan*

Gerhard Ziegmann − *Clausthal Centre for Material Technology, Clausthal University of Technology, 38678 Clausthal-Zellerfeld, Germany*

Complete contact information is available at: https://pubs.acs.org/10.1021/acsomega.3c10338

Author Contributions

All authors have given approval to the final version of the manuscript.

Notes

The authors declare no competing financial interest.

ACKNOWLEDGMENTS

The authors gracefully thank Dr. Dr.-Ing. Stephan Sprenger (Evonik Operations GmbH) for providing functionalized silica nanoparticles in MMA (Nanocryl XP 21 5235) for this work.

ABBREVIATIONS

ATR-IR, attenuated total reflection infrared spectroscopy; DLS, dynamic light scattering; DMF, *N*,*N*-dimethylformamide; EtOH, ethanol; FE-SEM, field emission scanning electron microscope; MMA, methyl methacrylate; PMMA, poly(methyl methacrylate); SEI, secondary electron image; TG-DTA, thermogravimetric differential thermal analysis

https://doi.org/10.1021/acsomega.3c10338
ACS Omega 2024, 9, 16279−16287

REFERENCES

(1) Plastics Europe. Plastics - the Facts 2021:An analysis of European plastics production, demand and waste data. https://plasticseurope.org/wp-content/uploads/2021/12/Plastics-the-Facts-2021-web-final.pdf (accessed 2022-05-26).

(2) Modulor GmbH. Polymethylmethacrylat (PMMA). https://www.modulor.de/werkstoffbibliothek/kunststoffe/polymethylmethacrylat-pmma/#:~:text=Laugen%20mittlerer%20Konzentration.-,Anwendung,Warndreiecken%2C%20Rücklichtern%20und%20Blinkergläsern%20verwendet (accessed 2022−06−14).

(3) Domininghaus, H.; Elsner, P.; Eyerer, P.; Hirth, T. *Kunststoffe*; Springer: Berlin Heidelberg, 2012 DOI: 10.1007/978-3-642-16173-5.

(4) Fullriede, H. Silica-Nanopartikel mit speziellen Eigenschaften für die Herstellung dentaler Kompositmaterialien, 2015.

(5) Kupke, P. Glas − und doch auch wieder nicht:KRD Sicherheitstechnik stellt neuen Verbundwerkstoff aus Glas mit Kunststoffkern vor. https://www.bm-online.de/produkte-und-tests/produkte/bauelemente2/glas-und-doch-auch-wieder-nicht/ (accessed 2022−05−27).

(6) Sattler GmbH. PMMA (Polymethylmethacrylat). https://www.sattler-scm.de/lexikon/pmma/ (accessed 2022−06−14).

(7) Rauch-Puntigam, H.; Völker, T. Acryl- und Methacrylverbindungen; Chemie, Physik und Technologie derKunststoffe. In EinzeldarstellungenSpringer, 1967; Vol. *9* DOI: 10.1007/978-3-642-46057-9.

(8) Goseki, R.; Ishizone, T. Poly(methyl methacrylate) (PMMA). In *Encyclopedia of Polymeric Nanomaterials*; Kobayashi, S.; Müllen, K., Eds.; Springer: Berlin Heidelberg, 2021; pp 1−11 DOI: 10.1007/978-3-642-36199-9_244-1.

(9) Yuan, M.; Huang, D.; Zhao, Y. Development of Synthesis and Application of High Molecular Weight Poly(Methyl Methacrylate). *Polymers* **2022**, *14* (13), 2632 DOI: 10.3390/polym14132632.

(10) Ali, U.; Karim, K. J. B. A.; Buang, N. A. A Review of the Properties and Applications of Poly (Methyl Methacrylate) (PMMA). *Polym. Rev.* **2015**, *55* (4), 678−705.

(11) Fixe, F.; Dufva, M.; Telleman, P.; Christensen, C. B. V. Functionalization of poly(methyl methacrylate) (PMMA) as a substrate for DNA microarrays. *Nucleic Acids Res.* **2004**, *32* (1), No. e9. Published Online: Jan. 12, 2004.

(12) Tao, S. L.; Lubeley, M. W.; Desai, T. A. Synthesis of cytoadhesive poly(methylmethacrylate) for applications in targeted drug delivery. *J. Biomed. Mater. Res., Part A* **2003**, *67A* (2), 369−375.

(13) Zhang, H.; Li, C.; Guo, J.; Zang, L.; Luo, J. In Situ Synthesis of Poly(methyl methacrylate)/SiO_2 Hybrid Nanocomposites via "Grafting Onto" Strategy Based on UV Irradiation in the Presence of Iron Aqueous Solution. *J. Nanomater.* **2012**, *2012* (4996), 1−9, DOI: 10.1155/2012/217412.

(14) Zou, D. Q.; Yoshida, H. Size effect of silica nanoparticles on thermal decomposition of PMMA. *J. Therm. Anal. Calorim.* **2010**, *99* (1), 21−26.

(15) Yang, F.; Nelson, G. L. PMMA/silica nanocomposite studies: Synthesis and properties. *J. Appl. Polym. Sci.* **2004**, *91* (6), 3844−3850.

(16) Zulfikar, M. A.; Wahab Mohammad, A.; Hilal, N. Preparation and characterization of novel porous PMMA-SiO2 hybrid membranes. *Desalination* **2006**, *192* (1−3), 262−270.

(17) Sriram, S.; Kumar, A. Separation of oil-water via porous PMMA/SiO_2 nanoparticles superhydrophobic surface. *Colloids Surf., A* **2019**, *563*, 271−279.

(18) Han, J.; Ma, G.; Nie, J. A facile fabrication of porous PMMA as a potential bone substitute. *Mater. Sci. Eng. C* **2011**, *31* (7), 1278−1284.

(19) Yoneda, S.; Han, W.; Hasegawa, U.; Uyama, H. Facile fabrication of poly(methyl methacrylate) monolith via thermally induced phase separation by utilizing unique cosolvency. *Polymer* **2014**, *55* (15), 3212−3216.

(20) Kanamori, K.; Hasegawa, J.; Nakanishi, K.; Hanada, T. Facile Synthesis of Macroporous Cross-Linked Methacrylate Gels by Atom Transfer Radical Polymerization. *Macromolecules* **2008**, *41* (19), 7186−7193.

(21) Suzuki, Y.; Onozato, S.; Shinagawa, Y.; Matsumoto, A. Microporous Structure Formation of Poly(methyl methacrylate) via Polymerization-Induced Phase Separation in the Presence of Poly(ethylene glycol). *ACS Omega* **2022**, *7* (43), 38933−38941.

(22) Sicher, A.; Ganz, R.; Menzel, A.; Messmer, D.; Panzarasa, G.; Feofilova, M.; Prum, R.; Style, R.; Saranathan, V.; Rossi, R.; Dufresne, E. Structural color from solid-state polymerization-induced phase separation. *Soft Matter* **2021**, *17*, 5772−5779.

(23) Chinthamanipeta, P. S.; Kobukata, S.; Nakata, H.; Shipp, D. A. Synthesis of poly(methyl methacrylate)−silica nanocomposites using methacrylate-functionalized silica nanoparticles and RAFT polymerization. In *Polymer*; Elsevier BV, 2008; Vol. *49*, 26, pp 5636−5642.

(24) Xu, L.; Zhang, X.; Chu, Z.; Wang, H.; Li, Y.; Shen, X.; Cai, L.; Shi, H.; Zhu, C.; Pan, J.; Pan, D. Temperature-Responsive Multilayer Films Based on Block Copolymer-Coated Silica Nanoparticles for Long-Term Release of Favipiravir. In *ACS Applied Nano Materials*; American Chemical Society (ACS), 2021; Vol. 4,12, pp 14014−14025.

(25) Xu, L.; Wang, H.; Chu, Z.; Cai, L.; Shi, H.; Zhu, C.; Pan, D.; Pan, J.; Fei, X.; Lei, Y. Temperature-Responsive Multilayer Films of Micelle-Based Composites for Controlled Release of a Third-Generation EGFR Inhibitor. In *ACS Applied Polymer Materials*; American Chemical Society (ACS), 2020; Vol. 2, 2, pp 741−750.

(26) Xu, L.; Chu, Z.; Zhang, J.; Cai, T.; Zhang, X.; Li, Y.; Wang, H.; Shen, X.; Cai, R.; Shi, H.; Zhu, C.; Pan, J.; Pan, D. Steric Effects in the Deposition Mode and Drug-Delivering Efficiency of Nanocapsule-Based Multilayer Films. In *ACS Omega*; American Chemical Society (ACS), 2022; Vol. 7, 34, pp 30321−30332.

(27) Sdrenka, S.; Schulz, M.; Marin, L. M.Modellierung, Herstellung und Evaluierung von Polymer-Protein-Kompositen mittels additiver Fertigungstechnologien *Düren* 2021 Shaker DOI: 10.21268/20210519-21.

(28) Liang, Y.; Ouyang, J.; Wang, H.; Wang, W.; Chui, P.; Sun, K. Synthesis and characterization of core−shell structured SiO_2@YVO_4:Yb^{3+},Er^{3+} microspheres. *Appl. Surf. Sci.* **2012**, *258*, 3689−3694, DOI: 10.1016/j.apsusc.2011.12.006.

(29) ISO 9277:2010 (2010): Determination of the specific surface area of solids by gas adsorption − BET method, Beuth-Verlag, Berlin, 2010.

(30) Thompson, E. V. Dependence of the glass transition temperature of poly(methyl methacrylate) on tacticity and molecular weight. *J. Polym. Sci. A-2 Polym. Phys.* **1966**, *4* (2), 199−208.

(31) Nikolaidis, A. K.; Achilias, D. S. Thermal Degradation Kinetics and Viscoelastic Behavior of Poly(Methyl Methacrylate)/Organo-modified Montmorillonite Nanocomposites Prepared via In Situ Bulk Radical Polymerization. *Polymers* **2018**, *10* (5), 491 DOI: 10.3390/polym10050491.

(32) Ferriol, M.; Gentilhomme, A.; Cochez, M.; Oget, N.; Mieloszynski, J. L. Thermal degradation of poly(methyl methacrylate) (PMMA): modelling of DTG and TG curves. *Polym. Degrad. Stab.* **2003**, *79* (2), 271−281.

(33) Christiansen, C. Untersuchungen über die optischen Eigenschaften von fein verteilten Körpern. *Erste Mittheilung. Ann. Phys.* **1884**, *23*, 298−306.

(34) Christiansen, C. Untersuchungen über die optischen Eigenschaften von fein verteilten Körpern. *Zweite Mittheilung. Ann. Phys.* **1885**, *24*, 439−446.

https://doi.org/10.1021/acsomega.3c10338
ACS Omega 2024, 9, 16279−16287